2011 IEEE/RSJ International Conference on
Intelligent Robots and Systems
September 25-30, 2011. San Francisco, CA, USA

An ultra-high precision, high bandwidth torque sensor for microrobotics applications

Benjamin M. Finio, Kevin C. Galloway and Robert J. Wood

***Abstract*— Motivated by the need for torque sensing in the μNm range for experiments with insect-sized flapping-wing robots, we present the design, fabrication and testing of a custom single-axis torque sensor. The micorobots in question are too large for MEMS force/torque sensors used for smaller live insects such as fruit flies, but too small to produce torques within the dynamic range of commercially available force/torque sensors. Our sensor consists of laser-machined Invar sheets that are assembled into a three dimensional beam. A capacitive displacement sensor is used to measure displacement of a target plate when the beam rotates, and the output voltage is correlated to applied torque. Sensor bandwidth, range, and resolution are designed to match the criteria of the robotic fly experiments while remaining insensitive to off-axis loads. We present a final sensor design with a range of $\pm$130μNm, a resolution of 4.5nNm, and bandwidth of 1kHz.**

I. INTRODUCTION

Within the last decade, multiple biologically-inspired robots have been developed at the insect scale, much smaller than traditional macro-scale robots yet larger than truly microscopic technologies such as MEMS (for examples see [1], [2]). The unique scale and operating conditions of these robots mean commercially available experimental tools may not always be sufficient and thus custom designs are required. For example, the robotic fly presented in [1] required the development of a two-axis force sensor to empirically determine lift and drag forces generated by the flapping wings [3].

More recent work on the robotic fly includes the use of asymmetric wing flapping motions to generate net body torques [4], where the magnitude of predicted torques is on the order of 1-10μNm. These values were obtained using a quasi-steady blade-element aerodynamic model [5] to predict aerodynamic forces and resulting body torques. To the authors' knowledge, even the most sensitive commercially available torque transducers fall short of the range, resolution and bandwidth demanded for microrobotic experiments. For instance, the Nano17 by ATI Industrial Automation (Apex, NC) offers a torque measurement capacity of 120mNm and a resolution near 16μNm, which is an order of magnitude too large for our application.

There have been several published works on the development and manufacture of custom torque sensors for a variety of applications. One micro-torque sensor developed for the watch industry [6] uses differential force measurement to achieve a resolution of 50nNm over a working range of $\pm$200μNm. The device consists of a spring blade positioned perpendicular to the torque axis (i.e. not mechanically connected) with a piezoresistive force sensor chip at both ends of the spring blade. A perpendicular bar mounted on the torque axis acts on the spring blade via two adjustment screws. These screws allow the spring blade to be pre-stressed so that an applied torque will increase pressure on one force sensor and decrease pressure on the other. While this micro-torque sensor has adequate range, its resolution falls short of our 10nNm target (discussed below).

The most relevant previous work was presented in [7] and improved upon in [8], where a contactless torque sensor was developed for rotating micromotors. The torque sensor in [8] uses a cross-shaped spring element where one end is fixed and the torque is calculated by measuring the torsional deformation at the free end with a laser triangulation sensor. The published sensing range was $\pm$200μNm with accuracy down to 4μNm. There are design features of this device, namely the cross-shape sensor beam, that are found in our proposed design, however, there are several key differences. The tests in [8] were purely static and thus dynamic behavior of the sensor itself was not a concern. The sensor rotation axis and motor shaft were directly aligned, therefore off-axis loading was not an issue. In our case, high-frequency actuation of microrobots can lead to both excitation of resonant modes of the sensor and high off-axis loads. Consequently, this raises issues related to the sensor's bandwidth, resolution, and off-axis stiffness among others which are rigorously addressed in Section II.

At the MEMS level there are some proposed designs that fall within our desired sensing range [9], [10], [11]. Still, this approach has it owns challenges including 1) a fragile building material (i.e. silicon) which makes sensor calibration and usage difficult, 2) extremely small mounting features, and 3) poor resistance to out of plane loads, especially for the type of cantilevered torque experiments we desire to run.

Other micro-torque sensors have been developed for characterizing micromotors [12], [13], [14], however, these devices were designed for continuously rotating motor shafts and are not easily adapted to measure body torques generated by flapping-wing microrobots.

This work was supported in part by the Army Research Laboratory (award number W911NF-08-2-0004), the Wyss Institute for Biologically Inspired Engineering, and the Department of Defense (DoD) through the National Defense Science & Engineering Graduate Fellowship (NDSEG) Program (Ben Finio).

The authors are with the School of Engineering and Applied Sciences and the Wyss Institute for Biologically Inspired Engineering, Harvard University, Cambridge, MA 02138. `bfinio@fas.harvard.edu`

978-1-61284-456-5/11/$26.00 ©2011 IEEE

II. SENSOR DESIGN

A. Criteria

The concept of the proposed single-axis torque sensor is that a solid structure should deform measurably when a torque is applied about the desired axis, but deformations should be negligible under other loading. The sensor geometry must meet this demand while simultaneously being realistic to manufacture. The deformation of the structure must then be converted into a useful electrical signal - frequently an analog voltage which is correlated to a torque value. The methods for measuring deformation typically fall under two categories: contact and contactless. Strain gauges and differential force measurement are examples of the former while capacitive sensors and laser inferometers fall within the latter category. Each method has its limitations with regards to range, bandwidth, and sensitivity, and must be selected appropriately in tandem with the design of the torque sensor.

The sensor must be designed such that its static and dynamic parameters are appropriate for the intended application, in this case torque measurements of a robotic fly. The sensor geometry must be designed such that deflection under expected torque loading applied by the fly is appropriate for the output mode selected. For example, capacitive sensors used to measure displacement will have both an upper bound due to limited range and a lower bound due to limited resolution, or the torque sensor itself could fracture or plastically deform under loading. A larger displacement will lead to better sensitivity for a given output mode, as long as the output is not saturated. The sensor's bandwidth must be sufficiently high such that its operation is ideally quasi-static in the expected frequency range of wing flapping. Unfortunately, these static and dynamic criteria conflict. A mechanically stiffer sensor will be less sensitive but will have a higher bandwidth; whereas a more compliant sensor will be more sensitive, but will have a lower bandwidth. Thus, there is an inherent tradeoff between sensitivity and bandwidth that must be considered in the design and is discussed in more detail below.

There are other, more qualitative criteria involving the three-dimensional arrangement of the sensor itself, robotic fly, and supporting structures. Design criteria are summarized here, quantitatively when possible:

1) **Sensor topology**: Compliant in the desired axis with high off-axis rejection ratio (at least 100:1)
2) **Manufacturability**: The sensor geometry must be practical to manufacture at the scale of an insect-sized vehicle
3) **Range**: At least ±100μNm, ten times the maximum expected torque output from a robotic fly
4) **Resolution**: Resolution of 10nNm, i.e. 0.01% of maximum torque range
5) **Bandwidth**: Sensor resonant frequency should be at least 1kHz (10 times the typical flapping frequency of 100Hz)
6) **Sensitivity**: ±100μNm should correspond to approximately ±10V analog output, i.e. a sensitivity of 100mV/μNm.
7) **Spatial considerations**: Sensor and supporting structure must avoid collisions with flapping wings and allow clear camera views for high-speed video of wing motions

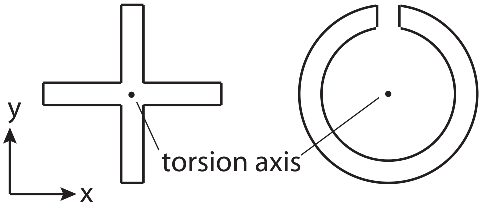

Fig. 1. Cantilever beams with cross (left) and slotted-tube (right) cross-sections are compliant to torques about the beam axis but insensitive to other loading.

These criteria are evaluated in detail below in order to arrive at a final sensor design. It is important to emphasize that many of the criteria are coupled. This therefore requires an iterative design process to converge on a solution that falls within the allowable limits of the design criteria.

B. Sensor Topology

As a starting point, we select a sensor topology. A cantilever beam with an appropriate cross section can serve to be compliant to a torque about the longitidunal beam axis, yet insensitive to torques about orthogonal axes and transverse or axial forces, (i.e. a high off-axis stiffness). A cross-shape cross section is analyzed in [15] as a suitable design for a flexible revolute joint due to its high off-axis stiffness. A "slotted tube", shown in Fig. 1, is also a viable option with high off-axis stiffness. We choose the cross-shaped design for purposes of manufacturability. Steel shim stock can be laser-machined in two dimensions and then assembled to form a three dimensional beam, similar to the process in [3], eliminating the need to machine a slit into a small metal tube. The cross-shape also has the advantage of being more symmetric to off-axis loading as compared to the slotted tube which is more sensitive to lateral forces in the x-direction than in the y-direction (axes defined in Fig. 1).

C. Output Mode

Capacitive sensors have proven useful in similar applications [3] due to their high sensitivity and bandwidth. A capacitive sensor consists of a probe head that forms a capacitor with an electrically grounded target plate. Motion of the target plate causes a measurable change in capacitance which is calibrated to displacement, force, or in this case, torque. Mounting a target plate to the edge of a cantilever beam allows measurement of the displacement of the plate when a torque is applied to the beam (Fig. 2). Despite their good bandwidth and sensitivity, capacitive sensors do have some drawbacks. One disadvantage is their typically small operating range (on the order of tens of microns), which requires very precise, parallel alignment of the probe

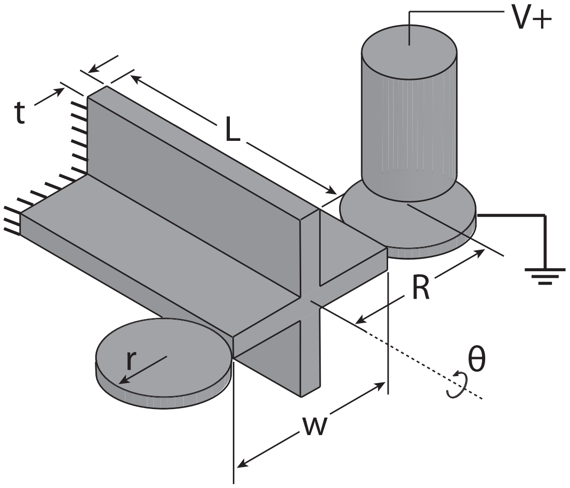

Fig. 2. Dimensions that define the sensor geometry. Electrical connections to the capacitive probe head and target plate are also shown.

head with the target plate. This small operating range also makes them susceptible to drift due to thermal expansion of components such as the sensor itself or surrounding support structures. The addition of a target plate also adds mass to the sensor, which will lower the mechanical resonant frequency of the beam and thus decrease the sensor bandwidth. Selection of capacitive sensors with appropriate specifications is discussed in Section III.

D. Analytical Model

The sensor geometry can be fully parameterized by the dimensions shown in Fig. 2: width w, thickness t, length L, target plate radius r and radius to the center of mass of the target plate R. We define R as a function of the width, target plate radius, and an additional offset d (i.e. the edge of the target plate does not necessarily need to abut the edge of the sensor beam, it can be cantilevered out on a support strut; this dimension is not shown in Fig. 2),

$$R = \frac{w}{2} + r + d \tag{1}$$

Given this geometry, [15] reports the torsional stiffness of such a beam as

$$k_\theta = \left(\frac{w}{t} - 0.373\right)\frac{4Gt^4}{3L} \tag{2}$$

where G is the shear modulus of the material. The total moment of inertia of the sensor about the θ axis is the sum of several components:

$$J_{tot} = J_{eq} + J_{ec} + J_{tp} + J_{fly} \tag{3}$$

where J_{eq} is the equivalent moment of inertia of the beam (since it is fixed at one end and twists along its length, this will be less than the moment of inertia of the beam as a rigid body), J_{ec} is the moment of inertia of the square end cap at the end of the beam (not pictured in Fig. 2), which serves as a flat surface to mount the device under test, J_{tp} is the moment of inertia of the target plates and support struts, and J_{fly} is the moment of inertia of the robotic fly and associated mounting hardware that will ultimately be attached to the end of the sensor. Note that by the parallel axis theorem, and accounting for both plates, J_{tp} is defined as

$$J_{tp} = 2\left(\frac{1}{4}mr^2 + mR^2\right) \tag{4}$$

The undamped resonant frequency of a spring-mass system is $\omega_n = \sqrt{k/m}$, so we have

$$f_n = \frac{1}{2\pi}\sqrt{\frac{k_\theta}{J_{total}}} \tag{5}$$

and we can use this as an approximation for sensor bandwidth (realistically the usable bandwidth will be lower than the resonant frequency). Next, for the static rotation θ of the sensor due to a torque τ applied by the fly, we have

$$\theta = \frac{\tau}{k_\theta} \tag{6}$$

and this rotation results in displacement δ_θ of the center of the target plate,

$$\delta_\theta = R\sin\theta \tag{7}$$

We also have the potential displacement of the target plate due to force F applied by the fly in the y direction,

$$\delta_y = \frac{F_y L^3}{3EI} \tag{8}$$

where I is the cross-sectional moment of area of the sensor beam. In order for the beam to effectively decouple torque and force measurements, we desire a high off-axis rejection ratio γ,

$$\gamma = \frac{\delta_\theta}{\delta_y} \tag{9}$$

for typical force and torque values F and τ expected from the fly.

Note that while δ_θ is the displacement of the *center* of the target plate, the target plate is actually undergoing translation and rotation. This could be a cause of concern for two reasons: (1) Capacitive sensors are typically designed and calibrated to measure displacements of parallel surfaces with a linear response, so the torque-to-voltage calibration could be nonlinear, and (2) the outer edge of the target plate will translate more than the center and could possibly collide with the probe head if the beam rotates too much. The latter concern can be alleviated simply through proper selection of geometric parameters; and while a linear calibration curve would be convenient, it is not necessarily required, thus this issue is not cause for excessive concern.

The concept of *sensor quality* is defined in [3] as the product of sensitivity and bandwidth, so in this case we have

$$Q = f_n \times \delta_\theta \tag{10}$$

since a higher f_n means a higher bandwidth and higher δ_θ means higher sensitivity. The quality factor is subject to two sets of constraints: (1) a minimum acceptable resonant frequency, determined by the expected frequency of the flapping tests, and (2) an acceptable range of target plate

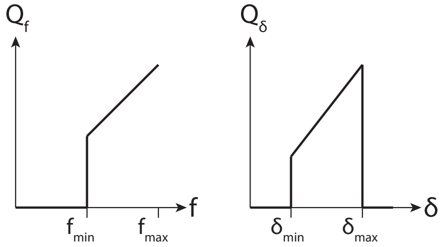

Fig. 3. Components of the quality factor Q, Q_f and Q_δ, are defined to be zero outside the acceptable ranges of frequency and target plate displacement.

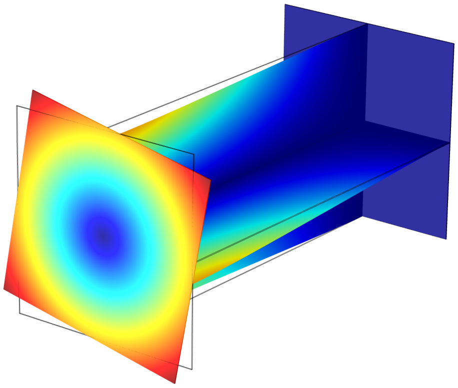

Fig. 4. A finite element model is used to predict static deflection under applied load, and vibrational modes of the beam.

displacements, determined by the range and resolution of the capacitive sensor. Designs outside of this range are not considered, which is equivalent to setting the quality factor to zero (Fig. 3).

E. Finite element model

In order to validate the analytical model, a finite-element model in Comsol (Fig. 4) is used to calculate the static rotation of the beam due to an applied torque as well as the first few resonant modes. Figure 5 shows that the static rotation of the beam and resonant frequency calculated by the numerical simulations match the analytical model very well for varying beam geometries (different lengths and widths for a fixed thickness, ignoring target plate and fly inertia for now). Therefore, we accept the validity of the analytical model and proceed to use it to select an optimal design, as this solution approach is much faster than running multiple finite element simulations over a wide range of geometries.

F. Optimization

The techniques used to fabricate the sensor (discussed below) allow sheets of metal shim stock to be machined to any dimensions L and w, however shim stock is only available in discrete thicknesses t (without the use of a lapping machine to thin down stock material). Thus for an available sheet thickness of $t = 152.4\mu$m we use the analytical model to calculate the target plate displacement δ_θ and resonant frequency f_n over a range of beam lengths and widths. Relevant physical parameters are given in Table I. Using a cutoff resonant frequency of $f_{min} = 1000Hz$ and allowable target plate displacements of $\delta_{min} = 0.5\mu m$ and $\delta_{max} = 10\mu m$ gives the allowable range of geometries (Fig. 6).

We select dimensions $w = 5mm$ and $L = 10mm$, which fall within the acceptable bounds. For these dimensions the beam resonant frequency is 1341Hz, the static torsion angle is 4.5×10^{-3} degrees, and the target plate displacement is $0.588\mu m$ (erring on the side of higher resonant frequency in case any inertias were underestimated). The predicted off-axis rejection ratio is $\gamma = 335$.

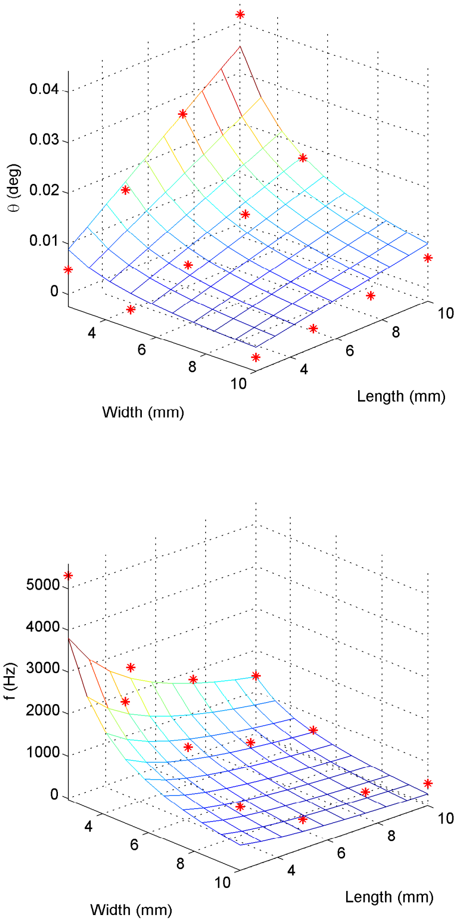

Fig. 5. Finite element model simulations (red markers) predict both static beam rotation (top) and first resonant frequencies (bottom) in agreement with the analytical model (mesh grid).

III. SENSOR FABRICATION

The sensor components are laser-machined from 6mil Invar shim stock using a 355nm diode-pumped solid state (DPSS) laser. Invar is selected due to its low coefficient of thermal expansion, in order to help mitigate calibration drift due to thermal expansion or contraction of the sensor beam. The 2D parts are then assembled (Fig. 7) and seams are

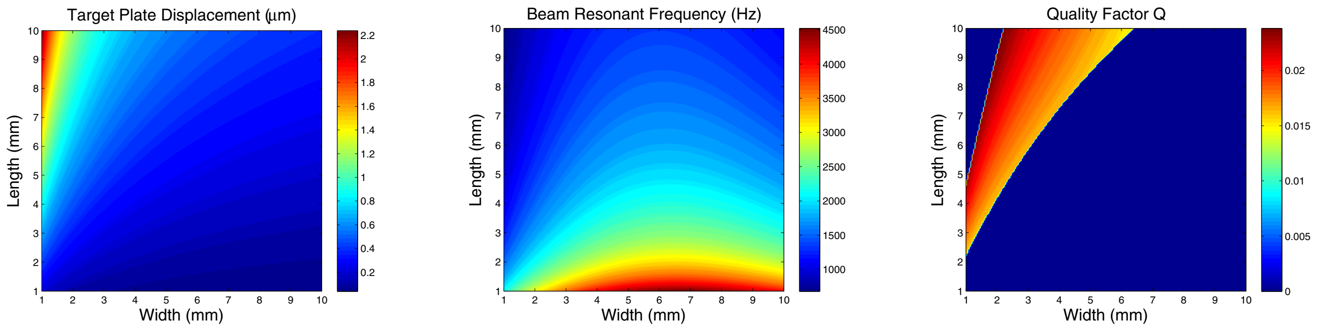

Fig. 6. Sensor target plate displacement (left), resonant frequency (center) and quality factor (right) as functions of beam length and width. The quality factor is set to zero outside of the acceptable displacement and frequency ranges, giving the acceptable set of geometries for the final design.

TABLE I

MATERIAL PROPERTIES AND OTHER PARAMETERS

Parameter	Variable	Value
Invar elastic modulus	E	141Gpa
Invar density	ρ	8,100kg/m^3
Invar Poisson's ratio	ν	0.29
Target plate radius	r	1mm
Target plate offset	d	4mm
Fly moment of inertia	J_{fly}	1.1μgm^2
Maximum torque from fly	τ	10μNm
Maximum lift from fly	F_y	120mg

laser-welded (Laserstar Technologies 1900 series). The high resolution of the laser machining system (roughly 5μm beam diameter) assures accurate assembly of the separate parts through mating features such as slots and tabs. The entire beam is laser-welded to a stainless steel block at the base, which is anchored to a base plate. Each capacitive sensor is mounted to a 5 DOF structure which allows precision alignment of the capacitive probe head with the target plate. The user has control over the capacitive sensor's X-Y-Z position, and a flexure mount holding the sensor offers up to 6° of pitch and yaw adjustability. While the system was designed with two target plates to allow differential readings from two separate capacitive sensors, the off-axis rejection ratio of the final design is high enough that only one sensor is necessary (a beam with a much lower off-axis rejection ratio and two capacitive sensors could serve as a dual lift/torque sensor). The capacitive sensor (Microsense model 8810 gauging system and model 2813 probe) was selected because the small probe diameter (2mm) allowed use of a smaller target plate, incurring less of a penalty on resonant frequency. The combined 8810/2813 system has a bandwidth of 10kHz, a range of $\pm 10\mu m$, and resolution of roughly 0.6nm. This range gives the torque sensor a factor of safety of roughly 17 to avoid overloading or output saturation, a resolution of over 1000 divisions of full-scale expected output (predicted maximum target plate displacement divided by capacitive sensor resolution), and enough bandwidth to collect up to 100 data points per flapping cycle for flapping at 100Hz. A CAD model and photograph of the completed assembly are shown in Fig. 8.

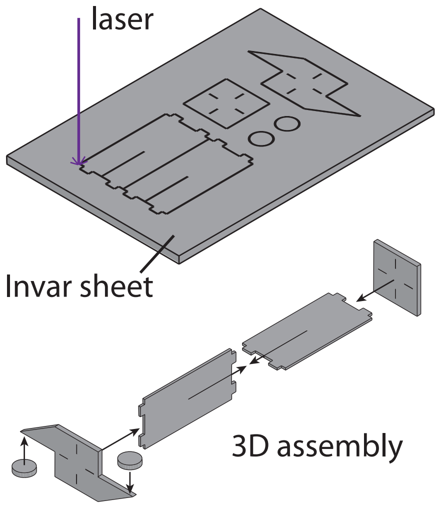

Fig. 7. Sensor beam components are machined in 2D with a laser (top) then assembled in three dimensions (bottom). Seams are laser-welded to join the pieces together. Refer to Fig. 2 for relevant dimensions of the final assembly.

IV. EXPERIMENTS

A. Static tests

For calibration, notches were laser-machined into the end cap of the beam at 1mm intervals that allowed calibration weights to be hung at varying radial positions. A small tray was also used to hang different weight combinations at the same radial position. All of these calibration curves are presented in Fig. 9 and show an average sensitivity of 75.8 mV/μNm. The zero level is subject to thermal drift with a time constant of several minutes (Fig. 10), but since flapping-wing experiments will occur in fractions of a second, as long as a new zero reading is taken immediately before each experiment, distortions of the data due to thermal effects can be eliminated.

B. Dynamic tests

The resonant frequencies of the beam with and without a robotic fly attached to the end are approximately 1.0kHz and 1.5kHz respectively, in close agreement with the analytical

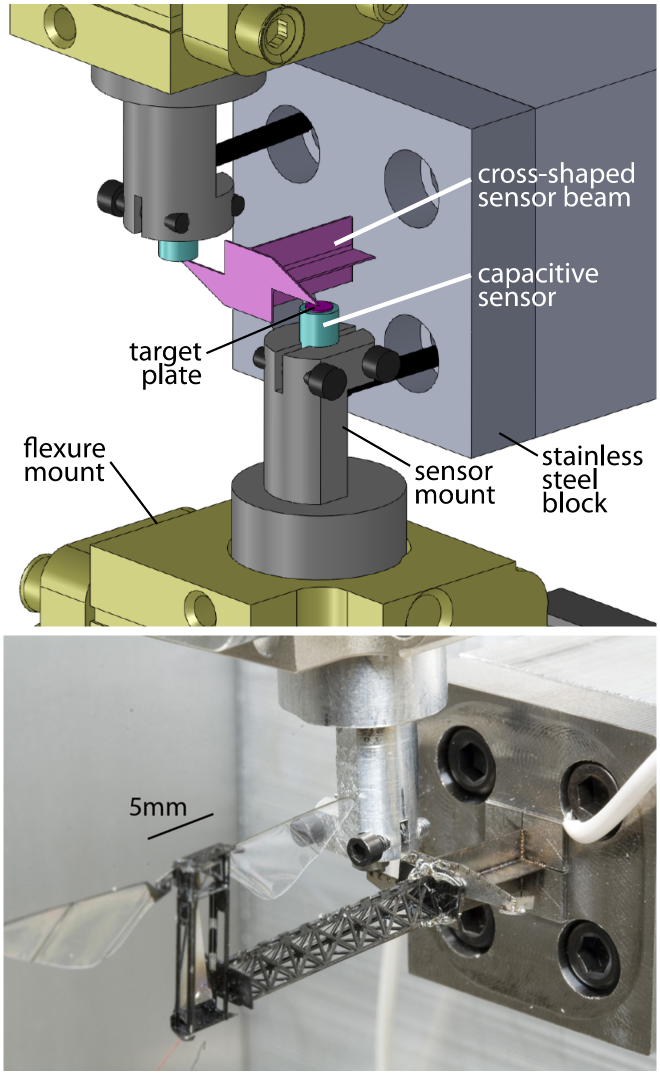

Fig. 8. A CAD model (top) of the completed assembly including sensor beam, capacitive sensors and supporting fixtures, and photograph (bottom) of the completed experimental setup with a robotic fly attached to the faceplate of the sensor via a lightweight carbon fiber truss structure (required to avoid collision of the wings and the capacitive sensor).

model and sufficient for flapping tests in the neighborhood of 100Hz. A 60mg robotic fly (a more recent prototype of the robot presented in [1]) was mounted to the end of the sensor in the configuration shown in Fig. 11. This orientation allowed measurement of pitch torques generated by the wings during flapping. The lift and drag forces both contribute to the net pitch torque. For symmetric upstroke/downstroke flapping, the contribution to pitch from the drag force over one stroke cycle should average out to zero. That is, flapping in one direction, the drag force is opposite the direction of wing motion and the contribution to pitch torque will be positive. When the wing reverses direction, the drag force also reverses direction and thus the contribution to pitch is negative. In general, the lift force always acts upward and does not reverse direction on the upstroke or downstroke (although lift values may briefly go negative near stroke

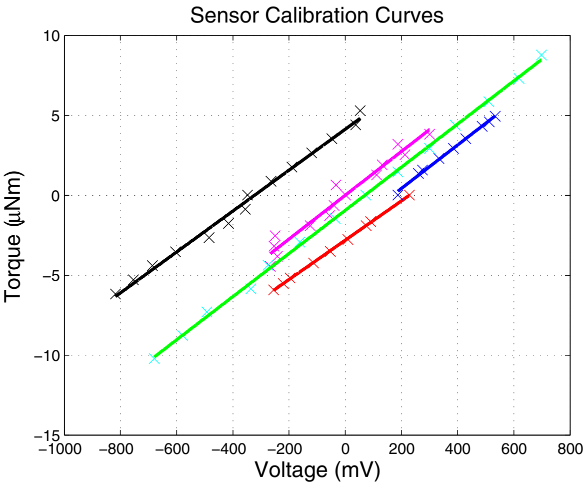

Fig. 9. Sensor calibration curves. Each color corresponds to a single calibration process (the entire process takes several minutes), with multiple calibrations taken over a period of hours or several days. The “x” markers correspond to individual readings, and each line is a linear least-squares fit. Multiple sensor calibrations show that while the zero reading is subject to drift over time, likely due to thermal effects, the sensitivity remains relatively constant.

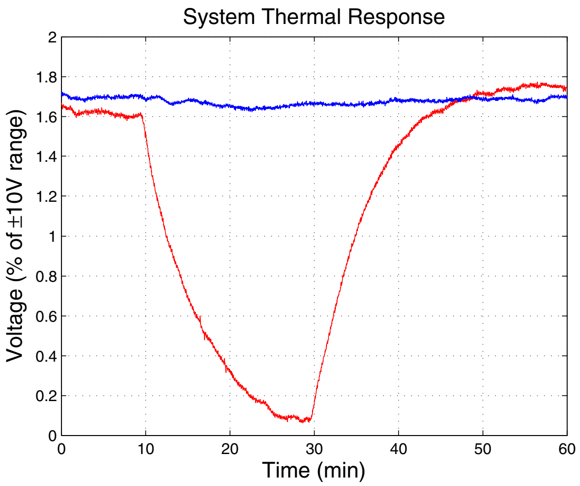

Fig. 10. The system is subject to drift due to thermal expansion, and over long time scales this can be significant due to ambient temperature changes or air currents in the room (blue). A fiber-optic light source aimed directly at the sensor was used to determine the system’s step response to a thermal input (red). The system’s thermal time constant τ is approximately 6.5 minutes, so it requires about half an hour to reach equilibrium. Significant changes in the thermal environment, such as bright lighting, can cause voltage drift on the order of several percent of the full operating range. This should be taken into account when collecting data.

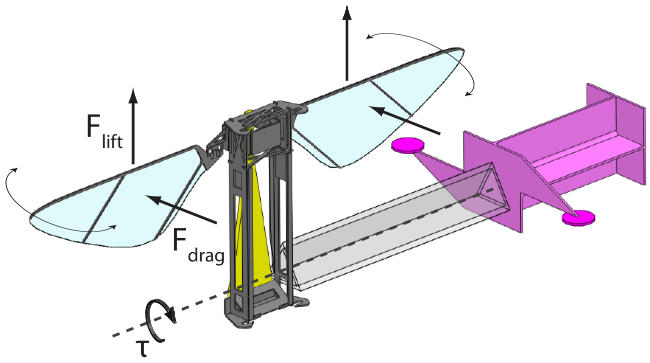

Fig. 11. The fly is mounted to the torque sensor in an orientation that allows measurement of pitch torques. Lift and drag forces act on the fly's wings as they flap back and forth, and both will contribute to the torque τ.

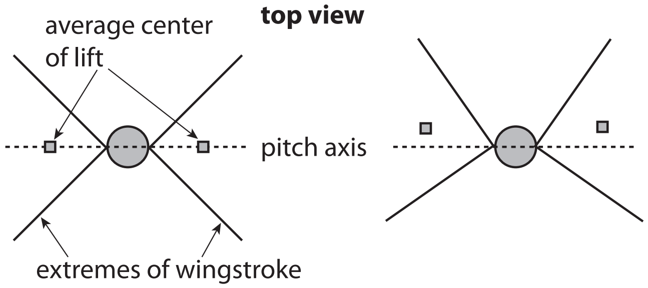

Fig. 12. Nominally, assuming a symmetric vehicle and symmetric upstroke and downstroke flapping, the center of lift (i.e., location of the average lift force over one wingstroke) will act in-line with the vehicle's center of mass, and there will be no pitch torque (left). However, biasing the stroke forward or backward while keeping the amplitude constant will move the point of action of the average lift force away from the pitch axis, generating a torque (right).

reversal due to inertial reactions, see [5]). Thus, changing the location of the average lift force vector over one stroke can change the average pitch torque acting on the vehicle (Fig. 12), and this fact will be useful for vehicle control and stabilization. For many small insects, the dynamics of wing flapping are typically an order of magnitude faster than body dynamics, therefore forces and torques averaged over several wingbeats can be sufficient for control purposes [16].

The robotic fly's wings are driven by a voltage-controlled piezoelectric actuator. To verify the proposed method for controlling average pitch torques, the wings were flapped at 100Hz with a drive signal amplitude of 200V, which corresponds to a stroke amplitude of approximately 100°, or a gain of 0.5°/V. The DC value of the control signal was varied over a range of ±25V, or about ±12.5° of stroke angle bias (note that these values are approximate - in future tests, stereoscopic imaging can be used to reconstruct exact wing position in 3D space, as in [5]). Instantaneous torque depends on contributions from both aerodynamic lift, drag and inertial forces (Fig. 11), however a running average (taken over ten wingbeats) shows a clear correlation between the offset voltage and the average torque value (Fig. 14). The sensor's high bandwidth allows characterization of contributions to torque with sub-period temporal resolution. If the resonant frequency of the sensor is sufficiently high relative to the flapping frequency, a low-pass filter can be used to eliminate signal components that arise due to sensor resonance (Fig. 13). When synchronized with wing kinematics, torque measurements would allow validation of aerodynamic models and decomposition of different contributions to net torque. This analysis is not presented here since 3D wing kinematics were not recorded, and for purposes of vehicle control, the important result is the time-averaged torque value.

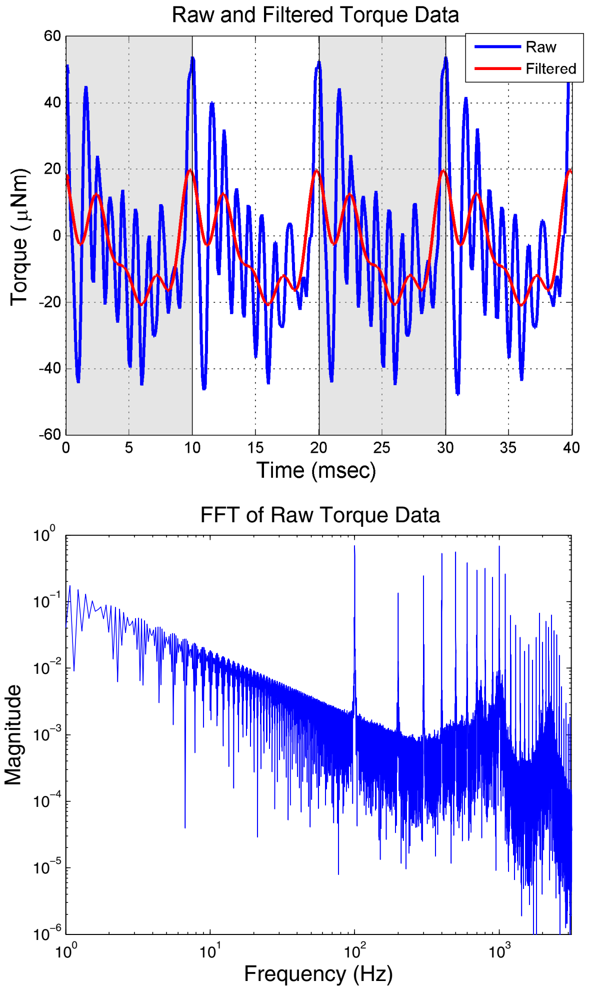

Fig. 13. (top) Instantaneous torque values have contributions from drag, lift and inertial forces and are also affected by sensor resonance. A tenth-order Butterworth filter with a cutoff frequency of 800Hz is used with the *filtfilt* command in Matlab to eliminate the high frequency components of the signal without adding a phase delay, which allows decomposition of torque readings on a sub-period basis. Data from four wingbeat periods is shown (one period = 10msec) for the baseline flapping case with zero offset voltage. (bottom) An FFT of the signal shows that there are strong components at both the flapping frequency (100Hz) and the sensor resonant frequency around 1kHz.

Flapping tests at 110Hz resulted in saturation of the ±10V analog output of the capacitive sensor, corresponding to a range of $\pm 130\mu$Nm. The final performance of the sensor is summarized in Table II.

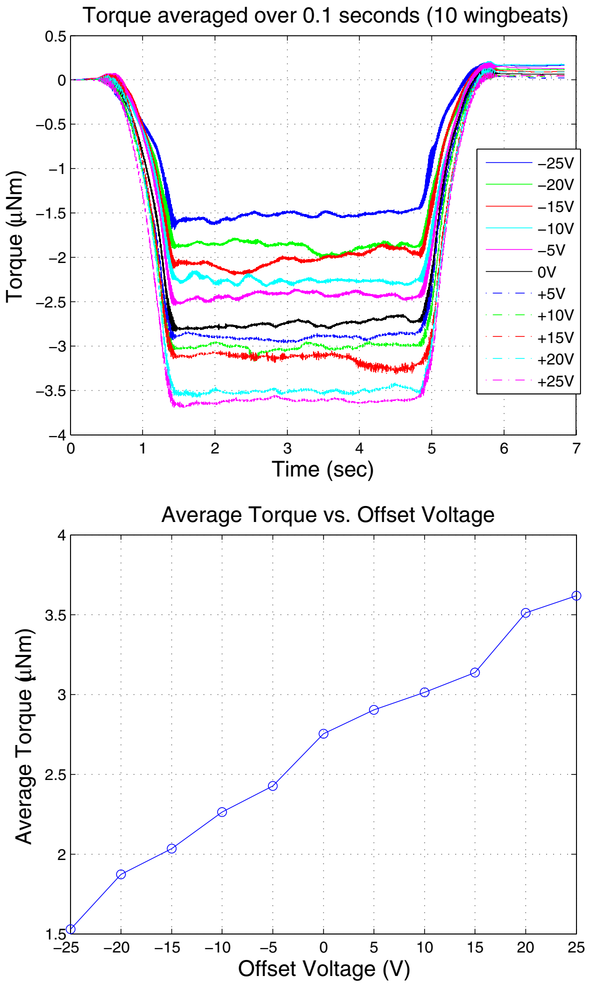

Fig. 14. (top) A running average taken over 0.1sec (10 wingbeats) shows that controlling the stroke angle offset via an offset voltage can directly control the DC value of the torque measurement. The transients at the beginning and end of the data are due to slow ramp-up and ramp-down of flapping to avoid damage to the device under test. (bottom) Correlating this average torque value to the offset voltage command shows a roughly linear relationship, which will be useful for developing control laws.

V. DISCUSSION

We have presented the analysis, design, fabrication and testing of a custom single-axis torque sensor suitable for measuring torques in a range not fulfilled by commercially available torque sensors. The final fabricated sensor has a range of ±130μNm, resolution of 4.5nNm and bandwidth of 1kHz. While the sensor was designed to meet criteria for a specific application - tests of a flapping-wing robotic fly - the geometry is scalable to meet different bandwidth or sensitivity criteria. It could easily be adapted to other applications such as measurements involving live insects or ambulatory microrobots. This concept can also be extended to more complex sensor geometries that can be used to measure multiple torques or force/torque combinations by designing a beam that is sensitive to additional forces or torques, although it becomes increasingly difficult to completely decouple motions as more degrees of freedom are introduced.

TABLE II
ACTUAL SENSOR PERFORMANCE

Parameter	Value
Off-axis rejection ratio	335
Range	±130μNm
Resolution	4.5nNm
Bandwidth	1kHz
Sensitivity	75.8mV/μNm

REFERENCES

[1] R. J. Wood, “The first takeoff of a biologically inspired at-scale robotic insect,” in *IEEE Trans. on Robotics*, vol. 24, 2008, pp. 341–347.

[2] A. Baisch, P. S. Sreetharan, and R. J. Wood, “Biologically inspired locomotion of an insect scale hexapod robot,” in *Intelligent Robots and Systems (IROS), 2010 In Proc. IEEE/RSJ Int. Conf. on*. IEEE, 2010.

[3] R. J. Wood, K. J. Cho, and K. Hoffman, “A novel multi-axis force sensor for microrobotics applications,” *Smart Materials and Structures*, vol. 18, p. 125002, 2009.

[4] B. M. Finio and R. J. Wood, “Distributed power and control actuation in the thoracic mechanics of a robotic insect,” *Bioinspiration & Biomimetics*, vol. 5, p. 045006, 2010.

[5] J. P. Whitney and R. J. Wood, “Aeromechanics of passive rotation in flapping flight,” *Journal of Fluid Mechanics*, vol. 1, no. 1, pp. 1–24, 2010.

[6] V. Gass, B. H. Van der Schoot, S. Jeanneret, and N. F. de Rooij, “Micro-torque sensor based on differential force measurement,” in *Proc. IEEE Int. Conf. on Micro Electro Mechanical Systems*, 1994, pp. 241 –244.

[7] F. Franek and A. Maciszewski, “Torsionselement und ver- wendung eines solchen bei einer einrichtung zur messung von reibungskraften,” Osterreichisches Patent AT 393 167 B, 1991.

[8] G. Abraham, R. Duffait, P. Wurmsdobler, A. Matzner, and W. Brenner, “Principles of torque measurement for rotating microactuators,” in *Sensors, 2002. Proceedings of IEEE*, vol. 2, 2002, pp. 1757 – 1761.

[9] A. Vujanic, N. Adamovic, M. Jakovljevic, W. Brenner, G. Popovic, and H. Detter, “Silicon microstructure for precise measurements of mechanical moments,” *Microelectronics Journal*, vol. 31, no. 11-12, p. 975 980, 2000.

[10] F. Beyeler, S. Muntwyler, Z. Nagy, M. Moser, and B. J. Nelson, “A multi-axis mems force-torque sensor for measuring the load on a microrobot actuated by magnetic fields,” in *Intelligent Robots and Systems. IROS IEEE/RSJ Int. Conf. on*, 2007, pp. 3803 –3808.

[11] F. Beyeler, S. Muntwyler, and B. J. Nelson, “A six-axis mems force-torque sensor with micro-newton and nano-newtonmeter resolution,” *Microelectromechanical Systems, Journal of*, vol. 18, no. 2, pp. 433–441, April 2009.

[12] H. Ota, T. Ohara, Y. Karata, S. Nakasima, and M. Takeda, “Novel micro torque measurement method for microdevices,” *Journal of Micromechanics and Microengineering*, vol. 11, no. 5, p. 595, 2001.

[13] C. Zwyssig, S. D. Round, and J. W. Kolar, “Analytical and experimental investigation of a low torque, ultra-high speed drive system,” in *Industry Applications Conf., 2006. 41st IAS Annual Meeting. Conf. Record of the 2006 IEEE*, vol. 3, oct. 2006, pp. 1507 –1513.

[14] D. Mathieson, B. J. Robertson, U. Beerschwinger, S. J. Yang, R. L. Reuben, A. J. Addlesee, J. Spencer, and R. A. Lawes, “Micro torque measurements for a prototype turbine,” *Journal of Micromechanics and Microengineering*, vol. 4, no. 3, p. 129, 1994. [Online]. Available: http://stacks.iop.org/0960-1317/4/i=3/a=006

[15] B. P. Trease, Y. M. Moon, and S. Kota, “Design of large-displacement compliant joints,” *Journal of Mechanical Design*, vol. 127, p. 788, 2005.

[16] X. Deng, L. Schenato, and S. Sastry, “Flapping flight for biomimetic robotic insects: Part II-flight control design,” *IEEE Trans. on Robotics*, vol. 22, no. 4, pp. 789–803, 2006.